HOSTED BY
ELSEVIER
Available online at www.sciencedirect.com
ScienceDirect
Soils and Foundations 63 (2023) 101268
SOILS AND FOUNDATIONS
www.elsevier.com/locate/sandf

Technical Paper

The behaviour of a low- to medium-density chalk under a wide range of pressure conditions

Tingfa Liu [a,b], Pedro M.V. Ferreira [c], Ken Vinck [d,*], Matthew R. Coop [c], Richard J. Jardine [d], Stavroula Kontoe [d,e]

[a] Department of Civil Engineering, University of Bristol, Queen's Building, BS8 1TR, Bristol, UK
[b] Formerly Department of Civil and Environmental Engineering, Imperial College London, Skempton Building, SW7 2AZ, London, UK
[c] Department of Civil Environmental and Geomatic Engineering, University College London, WC1E 6BT, London, UK
[d] Department of Civil and Environmental Engineering, Imperial College London, Skempton Building, SW7 2AZ, London, UK
[e] Department of Civil Engineering, University of Patras, Patras, Greece

Received 30 May 2022; received in revised form 14 November 2022; accepted 11 December 2022
Available online 26 December 2022

Abstract

Experiments are described which provided the basis for advanced numerical modelling of large-scale axial and lateral pile tests undertaken chalk to assist the design of offshore wind and other projects in northern Europe. The research explored the mechanical behaviour of chalk from a UK research site under effective cell pressures up to 12.8 MPa. When sheared from low confining pressures the chalk's interparticle bonds contribute a large proportion of the peak deviator stresses available to specimens that crack, bifurcate and dilate markedly after failing at relatively small strains. Progressively more ductile behaviour is seen as pressures are raised, with failures being delayed until increasingly large strains and stable critical states are attained. Loading invokes very stiff responses within the chalk's (Y_1) linear elastic limits and behaviour remains stiff, although non-linear, up to large-scale (Y_3) yield points. Near-elliptical Y_1 and Y_3 yield loci can be defined in q-p' stress space and a critical state v-p' curve is identified. The chalk's initially bonded, high porosity, structure is explored by normalising the shearing and compression state paths with reference to both critical state and intrinsic compression lines. The results have important implications for pile test analysis and practical design in this challenging geomaterial.

Keywords: Chalk; High-pressure; Triaxial; Stiffness; Yielding

1. Introduction

Chalk, a highly variable soft cemented biomicrite limestone, underlies large areas of North-West Europe, the Middle East and other regions, where it poses a series of series of challenges to geotechnical engineers; Mortimore (2012). Chalks with unconfined compressive strengths (UCS) of several MPa can stand in moderately high coastal cliffs. However, its response to foundation loading is hard to assess reliably because of its fissuring, brittleness and sensitivity (Lord et al., 2002). These features result in surprisingly low axial and lateral capacities for piles driven to support bridge, port, offshore and other structures at chalk sites. Pile driving leads to the chalk being 'de-structured' beneath pile tips and around their shafts during driving, with 'putty' annuli (with undrained shear strengths below 20 kPa) forming around their shafts (Lord et al., 2002). Uncertainties regarding the behaviour of intact and

Peer review under responsibility of The Japanese Geotechnical Society.
* Corresponding author.
E-mail addresses: tingfa.liu@bristol.ac.uk (T. Liu), p.ferreira@ucl.ac.uk (P.M.V. Ferreira), ken.vinck15@imperial.ac.uk (K. Vinck), m.coop@ucl.ac.uk (M.R. Coop), r.jardine@imperial.ac.uk (R.J. Jardine), skontoe@upatras.gr (S. Kontoe).

https://doi.org/10.1016/j.sandf.2022.101268
0038-0806/

'de-structured' chalk have imposed important limitations concerning the reliability and economy of foundation design for northern European offshore wind-turbine developments in for example Barbosa et al. (2017) or Buckley et al. (2020a).

These uncertainties led to the ALPACA and ALPACA Plus Joint Industry (JIP) programmes described by Jardine et al. (2019) involving dynamic, monotonic and cyclic axial-and-lateral field experiments on 41, mostly instrumented, piles driven in chalk. Piles with diameters ranging from 139 to 1800 mm were driven at the low- to medium-density St Nicholas at Wade (SNW, in Kent, UK) chalk research site where the overburden and weathered chalk had been removed, leaving intact Margate and Seaford units from the Upper Cretaceous Chalk Group. The very weak to weak strata were classified as having grades B2/B3 according to the widely used CIRIA chalk classification system (Lord et al. 2002). Vinck et al. (2022) describe their characterisation through in-situ profiling and laboratory testing on 102 mm diameter Geobore-S cores taken to 16 m depth and high-quality 350 × 350 × 250 mm blocks sampled from a 4 m deep excavation. Over 40 monotonic triaxial tests were conducted covering in-situ stress levels (mean effective stress p'_0 usually $<$ 150 kPa) and stresses 300 kPa higher; all failed at relatively small strains and showed brittle post-peak responses dominated by bifurcation and cracking. Parallel programmes of UCS, Direct Simple Shear, oedometer and Brazilian tests were also reported by Vinck et al. (2022).

A need was recognised to explore the chalk's behaviour under initial stresses significantly higher than those applied in-situ. The ALPACA piles mobilised tip pressures $>$ 10 MPa during compression testing and driving, triggering de-structuration and time-dependency that influenced shaft shear stresses during and after installation (Buckley et al., 2020a); lateral pressures $>$ 2 MPa were also mobilised during lateral loading pile tests (Pedone et al., 2020). Representative analysis and modelling of the pile load tests rely critically on the characterisation of chalk's small- and large-strain shearing behaviour under high stresses. This paper reports and interprets experiments run with p'_0 up to 12.8 MPa, referring to Leroueil & Vaughan's (1990) bonded geo-material framework, research on carbonate sands (Coop, 1990), very weak carbonate calcarenite rock (Lagioia & Nova, 1995; Cuccovillo & Coop, 1997a, 1999) and residual soils (Ferreira & Bica, 2006). One aim was to derive data which would allow the calibration of critical-state based constitutive models by Lagioia et al. (1996) and rate-dependent models, such as that described by Hickman & Gutierrez (2006) to capture the behaviour of chalk. Lagioia & Potts (1999, 2011) showed that representative numerical analyses of shallow foundation and tunnel problems can be made for comparably weak and brittle calcarenite rocks with such models. Fresh water-saturated chalk samples were tested in this study. Homand & Shao (2000) and Risnes (2001) demonstrated how chalk's mechanical behaviour varies with its saturating pore fluid (water, oil, or methanol). It is also well known also that chalk grains can be dissolved by Carbonic acid present in rain and groundwater, leading often to cavity features developing at onshore sites.

2. SNW chalk

The testing described below employed blocks from ≈ 1.8 m depth, in the layer that dominated the ALPACA piles' lateral loading response. Careful hand sampling mobilised, wherever possible, pre-existing fissures and bedding planes; all visibly fissured and weathered material was avoided. Vinck (2021) details the steps implemented to minimise sampling disturbance.

Multiple parallel triaxial tests on block samples from similar depths indicated variations of ± 12 % in in-situ undrained shear strength (S_u), as well as potentially concave pre-failure stress–strain curves (Vinck et al., 2022). Both features were interpreted as being due to optically identified, dominantly sub-vertical, micro-fissures set at ≈ 10 to 25 mm spacings. The near-saturated samples considered below had average bulk density of 1.92 Mg/m^3, porosity ≈ 45 %, natural water content ≈ 30 % and liquidity index ≈ 0.86. Tensiometer and piezometer measurements identified a water table 4.2 m below the main sampling level. Scanning electron microscopy (SEM) analyses by Alvarez-Borges et al. (2020) revealed open fabric with randomly assembled intact and broken coccoliths, coccolithic platelets and authigenic calcite grains. Inter-particle bonds were difficult to observe, suggesting relatively weak cementation (Clayton, 1983). Particle size analyses of chalk are affected by particle fracture, but Vinck's (2021) tests on manually ground-down dry chalk and de-structured putty (formed at the natural water content by laboratory compaction) both indicated well-graded fine silts with D_{50} around 3-4 μm.

Constant rate-of-strain (CRS) 1-D compression tests on SNW samples, illustrated in Fig. 1, confirmed trends identified in earlier studies into oil extraction-induced surface subsidence and well-borehole instability involving deeply buried chalks (Potts et al., 1988; Leddra, 1989). The natural chalk exists at void ratio-vertical effective stress (e-σ'_v) states that cannot be sustained by reconstituted samples (formed from slurry at 1.4 times the liquid limit). A log-linear K_0 post-yield intact compression line is also shown. Multiple stage-loaded oedometer tests on samples from all depths manifested very stiff, quasi-elastic, initial compression behaviour, with minimal volumetric straining before 'gross' yielding at stresses σ'_{vy} in the 4.5-7 MPa range, followed by steep volume reductions and compression indices (C_c) in the range of 0.18-0.5 that reflect bond rupture and potentially grain crushing, as commonly observed in granular media (see Altuhafi & Coop (2011)). The intact chalk's post-yield compression lines manifest

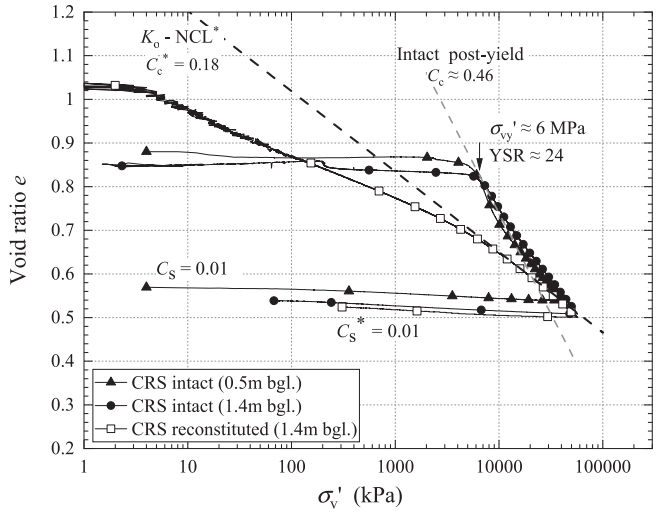

Fig. 1. Normal compression and post-yield compression lines identified for reconstituted and intact chalk; after Vinck (2021).

changes in their slopes and collapse towards the reconstituted intrinsic normal compression line (K_o-NCL*) as σ_v' reaches 30-50 MPa, as with calcarenites (Cuccovillo & Coop 1999). The intact and reconstituted specimens gave similar swelling indices on unloading from high pressures, reflecting breakage of the bonded chalk's micro-structure under high pressures.

3. Triaxial equipment, procedures and testing programme

3.1. Test equipment

Triaxial testing undertaken at Imperial College involved 38 mm diameter, 76 mm high specimens in computer-controlled Bishop and Wesley (1975) stress-path cells rated to 4 MPa deviatoric stresses (q) and 750 kPa cell and back pressures. The University College London experiments employed GDS (GDS, 2012) systems that could apply q up to 51 MPa and cell pressures up to 13 MPa to 50 mm diameter, 100 mm high specimens through digital pressure/volume controllers. The instruments' sensitivities, resolutions, and nominal precisions are summarised in Tables 1 and 2; laboratory temperatures were controlled to 21 (±1)°C.

Jardine et al. (1984), Kohata et al. (1997) and Tatsuoka et al. (1999) emphasise that high-resolution local sensors are essential to accurate geomaterial stiffness measurement. Local axial (vertical) strains were measured in both centres by 'floating' pairs of vertically mounted high-resolution LVDT transducers (Cuccovillo & Coop, 1997b). Calibrations confirmed that external measurements mis-recorded the chalk's strains and stiffnesses by factors of 10 or more, even at half peak deviator stress; see Fig. 2. Corrections were developed to correct external measurements by: (i) identifying system compliance, by subtracting from any linear test section exhibited by the external sensors the true local strain trend, and (ii) truncating the anomalously soft initial external q-ε_a section caused by eccentric loading and sample seating errors. The interpretation of the three highest pressure tests listed in Table 3 relied on corrected external measurements as their cell pressures exceeded the LVDT sensors' ratings. LVDT sensors often detach from specimens as failure develops, so the corrected external strain measurements were applied to the locally instrumented tests once $\varepsilon_a > 5$ %. As demonstrated later, depending on the initial effective stress level, specimens compressed to large strains ($\varepsilon_a > 30$ %) developed either inclined shear planes, bulging or transitional deformation between these two major failure patterns. Case-by-case, accurate area correction informed by continuous tracking of specimen deformation during shearing (through multi-level local radial strain sensors or optical visualisation via transparent cell walls) was not feasible in the current high-pressure experiments. Right-cylinder area correction was therefore retained as a consistent measure to derive global shear stresses.

Local radial strains are inherently more difficult to measure than axial (Ackerley et al., 2016). Liu (2018) describe how stick–slip and other local radial strain measurement problems were overcome in the low-pressure tests, but equivalent measurements proved difficult to achieve consistently in the high-pressure tests; the radial sensors failed to respond correctly in several cases. Reliance therefore had to be placed on corrected external volume measurements, which are affected by porous stone compliance, end imperfections, compression of drainage filter papers and compliance of the cell and connecting tubes. Stress-path specific compliance calibration tests were performed up to 13.5 MPa with a rigid stainless-steel dummy sample. The accumulated volume strain errors (ε_{vol}) exhibited moderately hysteretic patterns and could be linked with the applied stress p' (cell and back pressure difference) through a logarithmic function ε_{vol} (%) = -0.2 × ln(p') + 0.72. As demonstrated in later Fig. 3(a), the compliance-corrected external volume strains yielded representative bulk moduli ($K' = dp'/d\varepsilon_{vol}$) that matched broadly the locally measured trends over isotropic test stages. When required, the corrected ε_{vol}, ε_a and ε_r strain components were used to find deviatoric shear strain ε_s (=2(ε_a – ε_r)/3), as involved in stress-dilatancy interpretation shown later in Fig. 9.

3.2. Specimen preparation

Specimens were prepared by sub-dividing blocks or cores and encasing these in gypsum plaster to form rectangular blocks. The latter were clamped into a stable radial-arm coring machine equipped with diamond tipped drills and a water flushing system to remove chalk fragments/putty, ensuring smooth surface finishes. The cored samples were then enclosed in a split mould that was clamped in a metal-working lathe and the ends machined to satisfy tight flatness and parallelism tolerances, meeting or exceeding ASTM (2019) rock testing requirements. These steps are essential to representative stiffness, strength and post-

Table 1
Standard-pressure Bishop-Wesley type triaxial equipment: instrument type and performance.

Sensors /instruments	Full working range			Range & theoretical resolution				Precision *	
	Voltage	Travel	Sensitivity†	A/D range †	Limit	Range ‡	Resolution ‡	Variable	Stress/ strain
Cell /back /ram pressure sensors	50 mV	1000 kPa	0.05 mV/ kPa	1	400 kPa	0.4 MPa	0.01 kPa/bit	0.03 kPa	0.03 kPa
				2	1000 kPa	1.0 MPa	0.09 kPa/bit		
Load cell	28 mV	5 kN	5.6 mV/kN	1	3.7 kN	3.3 MPa	0.10 kPa/bit	0.14 N	0.12 kPa
				2	5 kN	4.4 MPa	0.75 kPa/bit		
Axial displacement transducer	35 mV	25 mm	1.4 mV/mm	1	14 mm	18.4 %	0.0006 %/bit	3×10^{-4} mm	4×10^{-4} %
				2	25 mm	32.9 %	0.0042 %/bit		
External volume-gauge	35 mV	50 cm^3	0.7 mV/cm^3	1	28 cm^3	32.5 %	0.001 %/bit	4×10^{-4} cm^3	5×10^{-4} %
Local axial LVDT §	±5 V	±5 mm	1000 mV/ mm	1	0.02 mm	0.04 %	1.2×10^{-6} %/ bit	3×10^{-5} mm	6×10^{-5} %
				2	0.15 mm	0.3 %	9.2×10^{-6} %/ bit		
				3	1.3 mm	2.6 %	7.9×10^{-5} %/ bit		
				4	5 mm	10 %	3.1×10^{-4} %/ bit		

Notes:
† Sensitivity based on amplified outputs; 16-bit A/D converter auto-range voltages: 1, 20 mV; 2, 150 mV; 3, 1.3 V; 4, 10 V;
‡ Values calculated for corresponding stress (σ_v, σ_h, q, in MPa) and strain (ε_a, ε_{vol}, in %) variables for typical specimen of 38 mm diameter, 76 mm height and LVDT gauge length of 50 mm;
* Expressed as standard deviation of 200 readings recorded prior to shearing with cell/back pressure of 350/300 kPa; presented in terms of measured variables and corresponding stress/strain.
§ Local radial strain measured with radial-belt type LVDTs with similar performance to that of the axial LVDTs, see Liu (2018).

failure measurement. The prepared test specimens' water contents remained close to their mean in-situ (≈ 29.7 %) value. Vinck (2021) confirmed initial suctions of 70 to 80 kPa on triaxial set-up and generally higher shear wave velocities than were measured in-situ by seismic CPT, suggesting minimal overall disturbance. Vinck et al. (2022) report on the degrees of variation seen between shear strengths and stiffnesses measured in parallel triaxial tests on 'standard' (38 mm diameter, 76 mm high) and 'larger' (100 mm diameter, 200 mm high) specimens. Their study indicates that the experiments described below on 38 mm and 50 mm diameter specimens may be compared without making any significant correction for their slightly different dimensions.

3.3. Triaxial testing procedures

Accurate determination of in-situ K_0 is challenging for SNW chalk due to the presence of open vertical fissures and disturbance by intrusive drilling. A low $K_o = 0.6$ was assumed for assessing in-situ stress after Lord et al. (2002), despite the chalk's Cretaceous age and very high yield stress ratios (YSR) (see Fig. 1). In-situ $p'_0 = 63$ kPa was estimated for the two lower-pressure triaxial tests based on unit weights and in-situ suctions measured by a tensiometer located 3 m above water table and ≈ 25 m away from the sampling pit.

The laboratory experiments did not attempt to reproduce chalk's complex sedimentary or post-sedimentary histories and applied instead isotropic consolidation stress paths. Table 3 lists the initial mean effective stresses p'_0 from which drained triaxial compression tests were undertaken to investigate the chalk's yielding in (compressive) triaxial effective stress-space.

Specimens were saturated by back pressures (300 kPa and 900 kPa in the low and high-pressure tests respectively) until Skempton's pore pressure coefficient B reached constant values > 0.95 before travelling on isotropic paths at 60 kPa/hour to the p'_0 target. The higher-pressure tests employed stages separated by 2-3 day pause periods that allowed volume straining associated with any excess pore pressure dissipation and creep to fall below 0.015 % per day. Drained monotonic axial compression followed, at a 5 %/day external strain rate, although the compliance errors shown in Fig. 2 led to far lower local rates until the chalk yielded. Some tests included post-failure stages where specimens were held undrained for 24 h at constant axial strain and cell pressure to examine the chalk's significantly time-dependent behaviour. Gradual unloading to zero cell pressure followed, without allowing drainage or axial straining, and observations were made of stress relaxation after shearing and undrained unloading, as discussed later.

4. Isotropic compression

The chalk's isotropic compression behaviour is summarised in Fig. 3(a) by the spread of (compliance-corrected) p'-ε_{vol} data from all tests, together with the broadly compatible bulk modulus trends assessed by assuming isotropic stiffness so that $\varepsilon_{vol} = 3$ times the ε_a strains measured with (higher resolution and more accurate) local axial strain sensors in the $p_0' < 3$ MPa tests.

Table 2
GDS 14 MPa high-pressure triaxial equipment: instrument type and performance.

Sensors /instruments	Full working range			Resolution *		Precision *	
	Voltage	Travel	Sensitivity	Variable	Stress/strain†	Variable	Stress/strain†
Cell /back /pore pressure sensors	100.1 mV	16.5 MPa	6.3 mV/MPa	0.1 kPa	0.1 kPa	1 kPa	1 kPa
Load cell	24 mV	100 kN	0.24 mV/kN	0.004 kN	2.0 kPa	0.0015 kN	0.76 kPa
Axial displacement transducer	80 mV	50 mm	1.6 mV/mm	0.002 mm	0.002 %	5×10^{-4} mm	5×10^{-4} %
External volume-gauge ‡	–	200 cm^3	–	0.2 mm^3	1×10^{-4} %	8 mm^3	0.004 %
Local axial/radial LVDT	±10 V	±5 mm	2000 mV/mm	1×10^{-4} mm	1.8×10^{-4} %	6.7×10^{-5} mm	1.2×10^{-4} %

Notes:
* Instrument resolution and precision varied with test stages and stress/strain levels; the values gauged from 200 readings recorded prior to shearing in a typical CID test with cell/back pressure of 2300/900 kPa;
† Determined for typical specimen of 50 mm diameter, 100 mm height and axial LVDT gauge length of 55 mm;
‡ Based on steps of an incremental motor integrated in a 16 MPa /200 cm^3 pressure/volume controller.

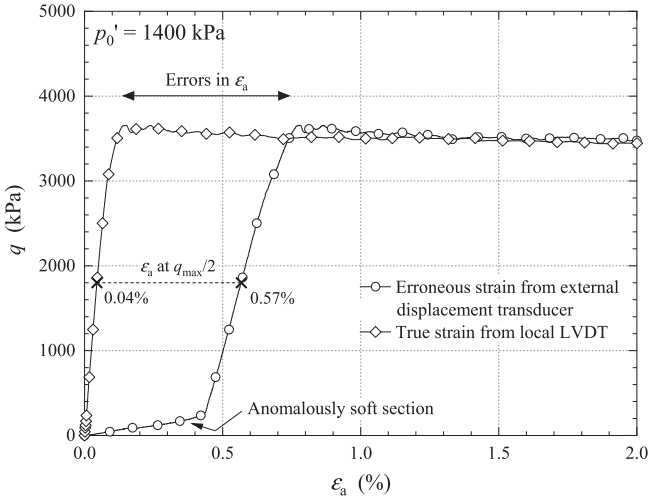

Fig. 2. Example test employed to calibrate compliance errors in external axial strains measured in the high pressure triaxial system.

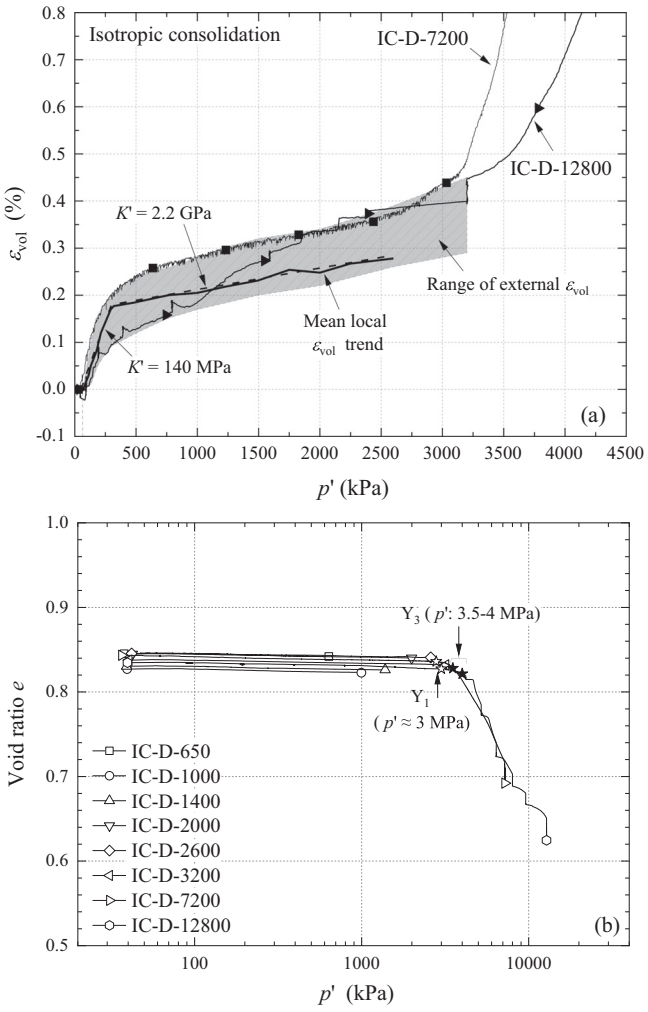

Fig. 3. Intact chalk isotropic compression behaviour: (a) local and corrected external ε_{vol} against p' and interpreted bulk stiffness trends; (b) e-p' response based on corrected ε_{vol}.

Drained probing tests by Vinck (2021) of the intact chalk's intial elastic behaviour showed that isotropic compresison to $p_0' > 350$ kPa leads to approximately isotropic stiffnesses, even though marked anisotropy is observed at lower pressures due to open micro-fissures. Fig. 3(b) presents the equivalent e-log p' plot; the key points are:

1. Relatively low initial $K' \approx 140$ MPa applied when $p' <$ 300 kPa, due probably to micro-fissures (Zimmerman, 1985), which appear to close tightly and allow K' to increase sharply to $\approx$ 2.2 GPa as pressures rise and remain steady until shortly before "gross" yielding led to steep K' reductions.
2. In the terms proposed by Jardine (1992) and Kuwano & Jardine (2007) and illustrated in Fig. 4, the end of the constant K' at $p' \approx 3$ MPa marks the point where the stress path engages a Y_1 kinematic yield surface which bounds the space within which the behaviour is linear elastic. The yield surface is subsequently dragged with the effective stress path and may be re-entered if the path reverses or changes its direction significantly.
3. The steepest rate of change in dK'/dp' applies at $p' \approx 3.5$-4 MPa, which is interpreted (within the same framework) as a 'Y_3' yield point. The post-Y_3 section of the highest-pressure test shows how the chalk de-structures as it travels along the post-yield compression line.

Table 3
Summary of test programme, listing test codes, specimens' typical initial diameter (D_0), height (H_0) and initial void ratios (e_0), triaxial specimens' prior to shearing void ratios (e) under isotropic stresses (p'_0) and oedometer specimens' maximum vertical stress ($\sigma'_{v,max}$).

Test code*	$D_0 \times H_0$ (mm)	e_0	e	p'_0 or $\sigma'_{v,max}$ (kPa)
IC-D-63	38 × 76	0.827	0.825	63
IC-D-363	38 × 76	0.827	0.823	363
IC-D-650	50 × 100	0.845	0.842	650
IC-D-1000	50 × 100	0.827	0.823	1000
IC-D-1400	50 × 100	0.830	0.826	1400
IC-D-2000	50 × 100	0.844	0.840	2000
IC-D-2600	50 × 100	0.845	0.841	2600
IC-D-3200	50 × 100	0.838	0.832	3200
IC-D-7200	50 × 100	0.843	0.692	7200
IC-D-12800	50 × 100	0.834	0.624	12,800
CRS-I-0.5	38 × 20	0.880	–	42,900
CRS-I-1.4	38 × 20	0.848	–	56,800
CRS-R-1.4	38 × 20	1.032	–	56,800

Notes:
* Test code: I – intact chalk; R – Reconstituted chalk; C – triaxial compression; D – drained shearing; CRS – Constant rate-of-strain compression.

4. Delayed consolidation and creep straining became increasingly significant over all consolidation pause periods imposed with $p' \geq 3.2$ MPa.

5. Shearing to failure

5.1. Shear stress-strain response

The tests are divided into three groups based on their pressure ranges:

Group A: $p'_0 = 63$ to 363 kPa.
Group B: $p'_0 = 650$ to 1400 kPa.
Group C: $p'_0 = 2.0$ to 12.8 MPa.

Fig. 5(a-c) plots their stress–strain responses up to 0.5 % axial strain. Y_1 yield points are shown to mark the ends of any initial linear portions, as are Y_3 points at the mid-points of the large-scale yielding stages where marked changes in stress–strain response occur. As shown later, the experiments did not provide any systematic indication of Y_2 yielding which was located by Jardine (1992), Smith et al. (1992), Kuwano & Jardine (2007), Gasparre et al. (2007) and Liu (2018) in clays and sands as the points where abrupt changes in strain increment directions and the development of strain rate dependency occur in drained shearing tests. These changes were interpreted as reflecting the onset of particle contact phenomena that are not expected to apply to more strongly cemented geomaterials. The identified yield stresses and corresponding axial strains are listed in Table 4. The initial linear stress–strain curves condense into relatively narrow ranges up to $\varepsilon_a = 0.05$ % for each group. As discussed later, similar maximum values of vertical stiffnesses E_v' applied in each set, with pressure-dependent Poisson's ratios (v'_{vh}) between 0 and 0.25.

The chalk's response depended markedly on pressure. Group A specimens reached their peak strengths (q_f) with $\varepsilon_a < 0.1$ % before fracturing and collapsing towards discontinuous assemblies of blocks and fragments. Increasing p'_0 led to disproportionately small increases in q_f in Group B; raising p'_0 from 63 kPa to 1.4 MPa led to only a 60 % gain in peak resistance. However, the degree of brittleness reduced with increasing p'_0 and Group C's response was ductile or strain hardening. The gradual transition from brittle to ductile behaviour is explored in terms of the effective stress ratio (q/p') in Fig. 6 and illustrated by the failure patterns identified in Fig. 7. Further points to note include:

1. Group A specimens' peak q/p' ratios approached 3, the no-tension ratio. Tests conducted from in-situ stresses often developed vertical cracks and shear discontinuities that call into question late-stage test interpretation in terms of 'continuum-mechanics' invariant q/p' parameters. Resolving the shear and normal stresses acting on shear planes (measured after testing to be inclined at around 60-65° to the horizontal) to assess operational shear strengths, as recommended by Burland (1990) indicates ultimate ϕ' values of 30 to 40° when c' is assumed = 0 (Vinck et al., 2022).
2. Group C tests were ductile with $(q/p')_{ult} \approx 1.25$, equivalent to critical state ϕ' values of ≈ 31°, as seen also with fully de-structured chalk (Doughty et al., 2018; Liu et al., 2022) or sub-rounded fine silica sands (Aghakouchak et al., 2015).
3. Group B tests developed intermediate peak stress ratios that reduced systematically as p' increased and tended to fall, post-peak, towards $(q/p')_{ult} \approx 1.25$.

5.2. Volumetric strains

The ten shear tests' global volume and axial strain development, as presented in Fig. 8, indicate marked changes in dilatancy with increasing p'_0. The $p'_0 = 63$ kPa test devel-

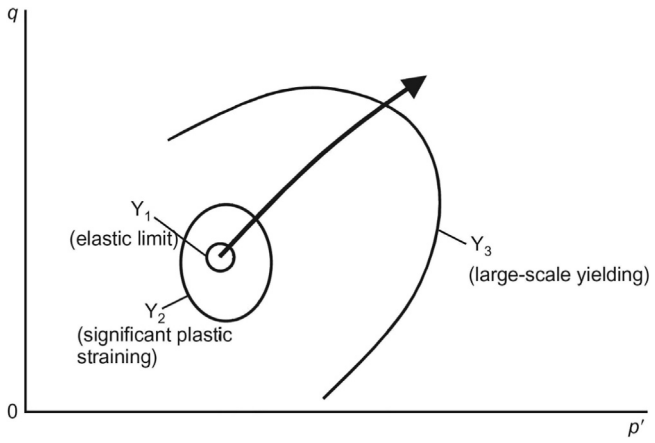

Fig. 4. Illustration of multiple yield surface scheme (revised from Jardine (1992), Kuwano & Jardine (2007)).

oped minor contractive (positive) volumetric strain (≈ 0.07 %) up to its peak strength, followed by marked 'dilation' as the specimen bifurcated and cracked. Similar patterns were reflected in parallel undrained tests' pore pressures (Vinck et al., 2022). Group B specimens exhibited (positive) volumetric strains, following a broad pattern of void ratio reductions increasing with confining pressures, reaching 6 % contractive straining after 35 % axial strain in the $p'_0 = 1400$ kPa experiment. The volumetric compressions of the Group C specimens appeared to condense into a narrower range that tended towards volumetric strains of 12-14 %. The total strains can be further decomposed to consider the elastic and plastic components, noting the bulk moduli (K') established in Fig. 3(a) and the maximum Young's moduli ($E'_{v,max}$) discussed later, and assuming these moduli remained constant as shearing evolved. Table 5 summarises the plastic axial and volumetric strains as proportions of the corresponding total strains ($\varepsilon_a^p/\varepsilon_a^t$, $\varepsilon_{vol}^p/\varepsilon_{vol}^t$), considering the conditions applying at the Y_3 yield points. Elastic axial straining dominated up to Y_3 in the lowest pressure test (IC-D-63), although it manifested dilative plastic volumetric strains from an early stage of shearing due, we argue, to its system of partially open microfractures. These micro-fissures close under higher pressures, suppressing this apparently dilative trend. The plastic strain components are more important in the higher pressure tests where they make up, on average, around 42 % and 80 % of the total axial and volumetric strains respectively at the points of Y_3 yielding and become dominant beyond these points.

The corresponding q/p' - $d\varepsilon_{vol}/d\varepsilon_s$ stress-dilatancy relationship is plotted in Fig. 9. Also shown are the Y_1 and Y_3 yield points. No distinct change in the traces' curvature between these points is observed that signifies possible intermediate Y_2 yielding. The $p'_0 = 63$ kPa test showed dilatancy from an early stage of shearing, as is common with rocks, probably reflecting their micro-fissures (Cerfontaine & Collin, 2018). Group B specimens appeared to show strain increment direction changes well before reaching Y_1 yielding stages, while the great scatter in the Group C tests' early stages reflect the absence of local strain measurements. Average Poisson's ratios v'_{vh} of 0.25,

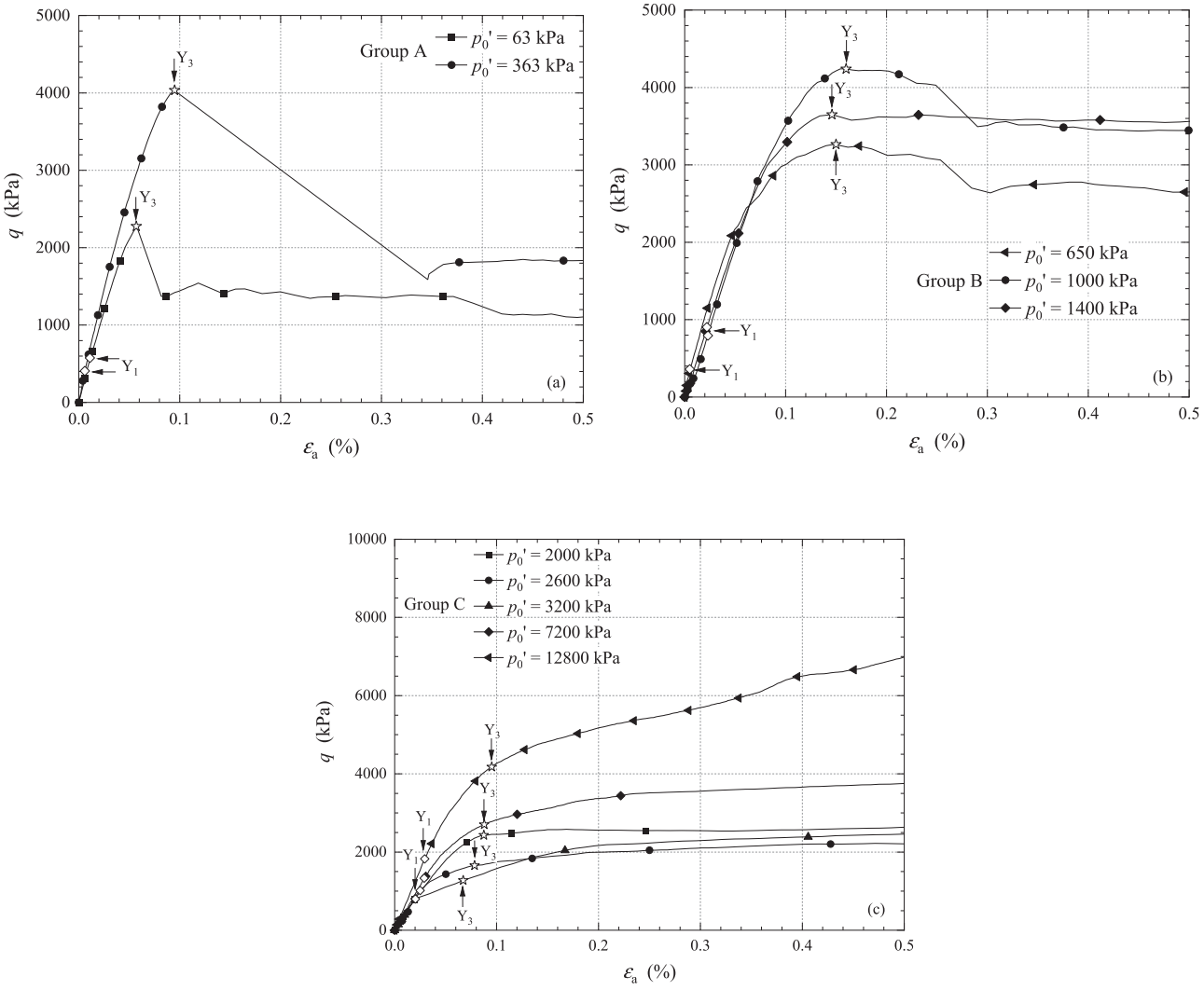

Fig. 5. Deviatoric stress-axial strain trends over small strain range: (a) Group A; (b) Group B; (c) Group C.

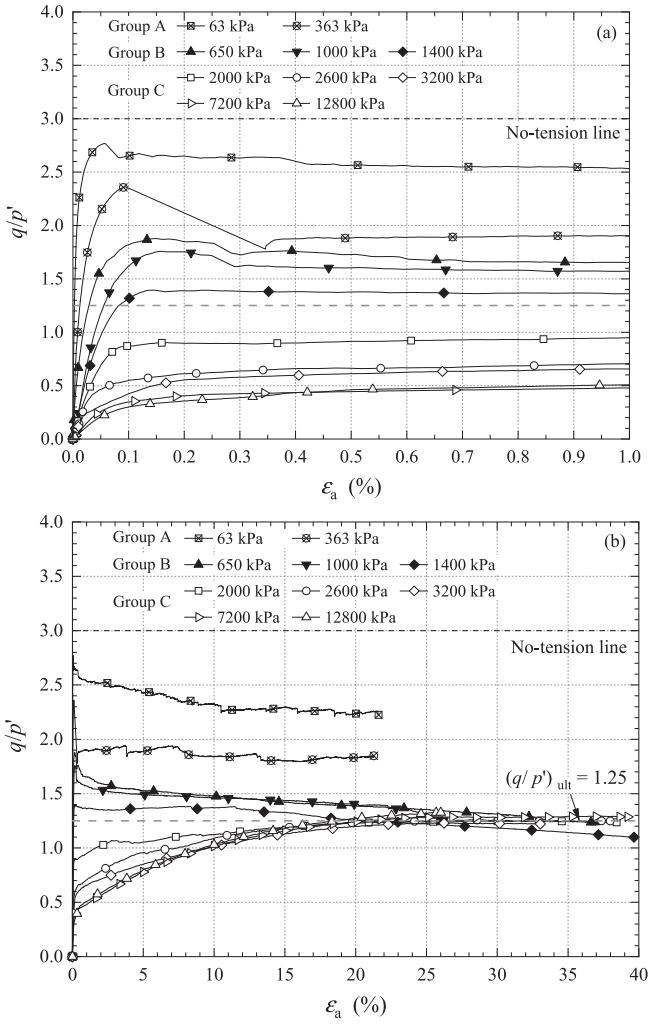

Fig. 6. Stress ratio (q/p') against axial strain trends: (a) zoomed-in initial 1% axial strain range; (b) full strain range.

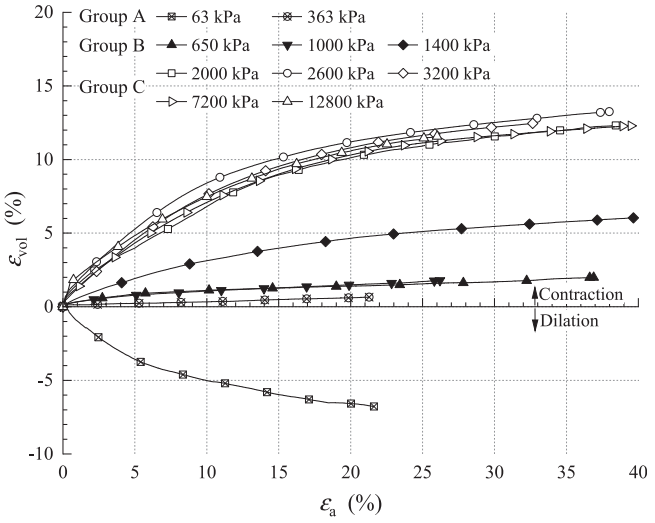

Fig. 8. Volumetric strain evolution trends over full axial strain range.

0.20 and 0 were interpreted for the Group A, B and C effective stress ranges respectively. All specimens developed their q/p' peaks while undergoing volumetric contraction; only the $p_0' = 63$ kPa test dilated post-peak. Group B specimens approached critical states with $d\varepsilon_{vol}/d\varepsilon_s$ decreasing towards zero, while the ductile Group C specimens exhibited strain-hardening behaviour and headed towards critical states. Overall, the chalk's stress-dilatancy characteristics resemble those of weak calcarenite (Cuccovillo & Coop, 1999).

5.3. Peak shear strength envelopes

The chalk's peak strength envelope is curved, leading to shear strength parameters that vary markedly with pressure. Vinck et al. (2022) adopted a pressure-dependent

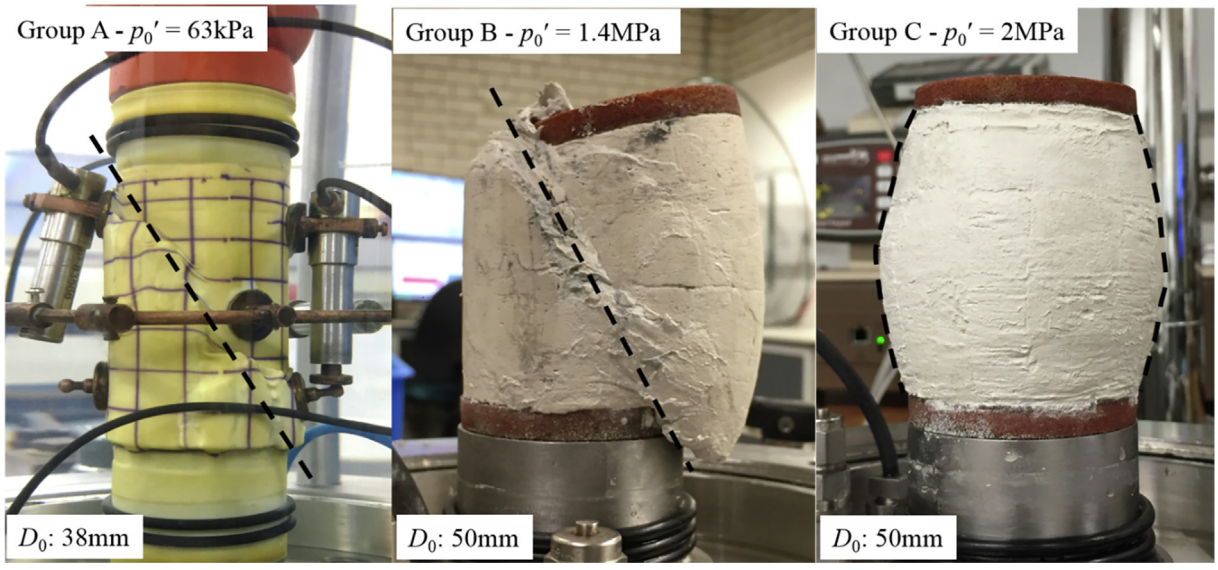

Fig. 7. Failure characteristics of intact chalk specimens.

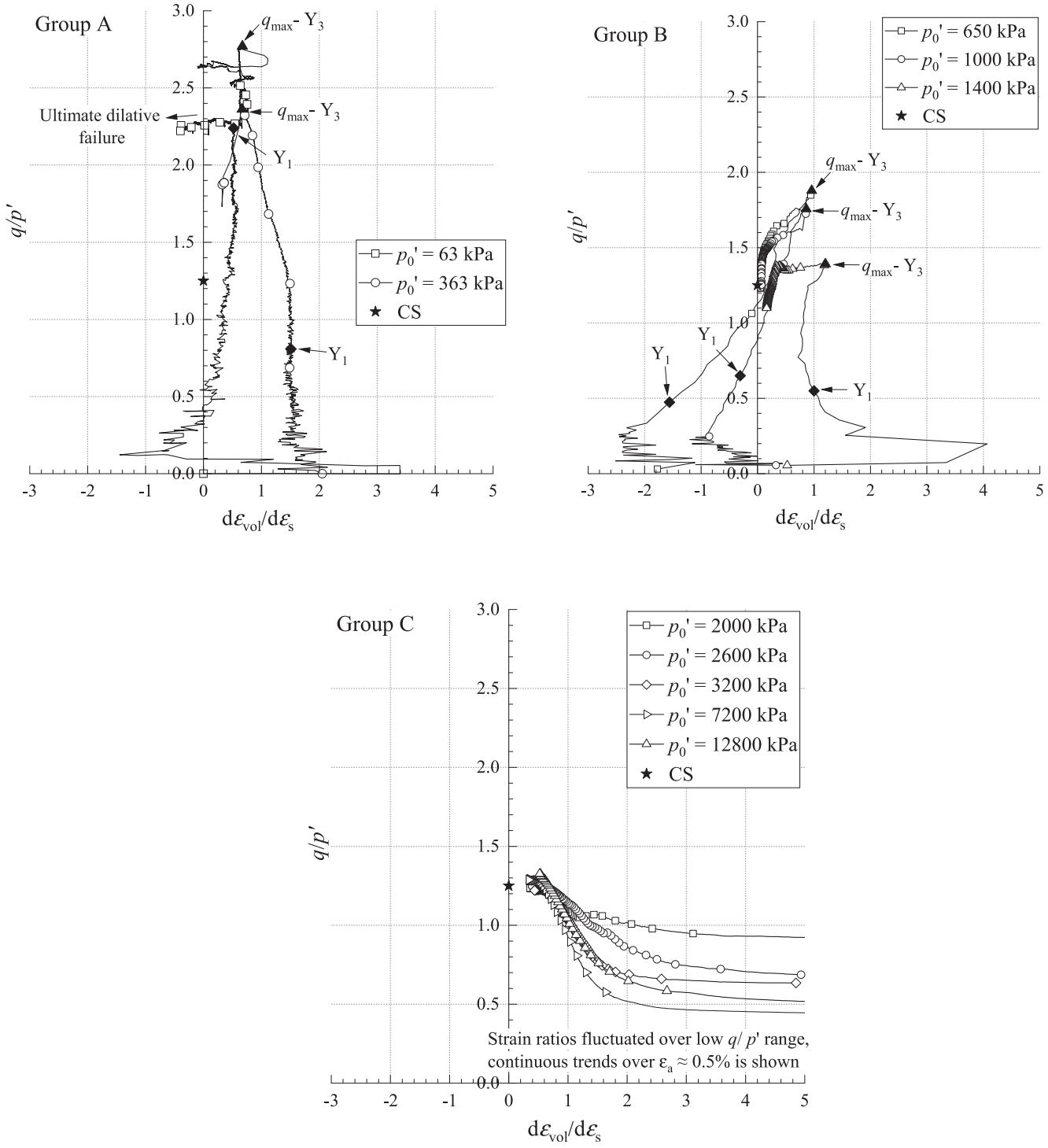

Fig. 9. Stress dilatancy correlation of intact chalk.

Mohr-Coulomb model to distinguish broadly how intact chalk's 'bonded' and 'frictional' components of strength varied with pressure level. They combined drained and undrained (CID and CIU) triaxial tests to interpret a representative intact peak Mohr-Coulomb envelope for SNW covering the low in-situ p_0' (< 150 kPa) to p_0' + 300 kPa pressure range with a $c' = 490$ kPa and $\phi'_{peak} = 39.6°$ envelope which is re-plotted on Fig. 10 along with the higher p_0' test outcomes. The 'low-pressure' tests' relatively high apparent cohesion component reflects the level of inter-particle bonding between the cemented silt-sized calcium carbonate ($CaCO_3$) aggregates, but it is not synonymous with the true component of bonded shear strength, which could not be identified directly from the Authors' experiments. The lowest p_0' tests developed peak strengths situated marginally to the right of the $\sigma_3' = 0$ and $q/p' = 3$

zero radial effective stress (no tension) limit that applies in all triaxial tests. Increasing p'_0 clearly weakens inter-grain bonding and promotes a more 'frictional' response to shearing. All tests showing peak $q/p' > M = 1.25$ softened post-peak and headed towards this ultimate, critical state, ratio. The failure patterns shown previously in Fig. 7 reflected the same processes. While variations between specimens led to a range of low-pressure brittle bifurcation patterns, most tended to form shear zones inclined at 60-65° to the horizontal. The ductile Group C specimens formed bulging failures and delivered markedly reduced post-test water contents (16–23 %), while Group B specimens developed both radial bulging and formed 6-8 mm thick bands of remoulded chalk within diffused shear zones inclined ≈ 65° to the horizontal.

The peak triaxial compressive shear strengths of bonded weak rocks are relatively insensitive to consolidation paths applied within their Y_3 envelopes (Leroueil & Vaughan 1990). But they generally offer far lower strengths in tension. Vinck et al. (2022) confirm that far lower shear strengths and stiffness apply to chalk in tests that induce tensile failure. Their Brazilian tension strengths were 90 % lower than the UCS values, while the direct simple shear (DSS) strengths were 50 % lower than those in triaxial compression. Further hollow cylinder apparatus (HCA) and high-pressure extension testing is warranted to investigate chalk's potentially stress-path dependent and anisotropic mechanical behaviour.

5.4. State paths during shearing

The $p'_0 \geq 1$ MPa tests all displayed no visible fracturing and followed the compressive v-p' state paths (where $v = 1 + e$) indicated in Fig. 11. Test IC-D-12800 halted slightly prematurely, as indicated in Fig. 6(b), and its end point was extrapolated marginally to match the conditions at 40 % axial strain, following Ferreira & Bica's (2006) procedure. The path ends scatter around a log-linear relationship, which is taken as the critical state line with $\Gamma = 2.74$ and $\lambda = 0.134$. Fig. 11 also re-plots from Fig. 3(b) the intact chalk's post-Y_3 isotropic compression line with $N = 3.14$ and $\lambda = 0.16$. Also plotted for comparison are the post-yield isotropic compression and critical state lines for the intact chalk, the normal compression line for reconstituted chalk and the (common) critical state line established from tests on reconstituted and fully de-structured chalk by Liu et al. (2022). The log-linear isotropic-NCL* was constructed from the K_o-NCL* shown in Fig. 1, taking $\phi' = 31°$ and $K'_o = 1 - \sin\phi' = 0.48$ when $OCR = 1$. It is interesting to note the intact chalk's critical state line runs at a steeper slope (higher λ) than that of the dynamically compacted fully de-structured chalk reported by Liu et al. (2022), reflecting intact chalk's progressive de-structuration under isotropic compression and shearing, as observed and modelled with crushable granular media (Altuhafi et al., 2017; Ciantia et al., 2019). It may be speculated that the critical state lines of intact and de-structured chalk converge over even higher consolidation and shearing stress ranges as the de-structuration process terminates fully.

5.5. Stress relaxation after shearing and undrained unloading

As noted earlier and shown by Buckley et al. (2020b), large-strain, high-pressure, shearing occurs in pile tips during driving that leads to very low strength putty annuli forming around their shafts under low mean effective stresses and tightly kinematically controlled (near zero volume change) conditions (Jardine, 2020). Final stages were incorporated into some high-pressure tests to try to match aspects of the regime within the putty annuli. These final stages were applied after undergoing large strain, high-pressure, shearing. The specimens were then held (undrained) under constant axial strain and cell pressure over extended pause periods. Fig. 12 shows how the deviatoric stress (q) relaxed by 26 %, or 700 kPa, over 24 hours in IC-D-1400 (the highest-pressure Group B test) after achieving its $q_{ult} \approx 2.7$ MPa critical state resistance. Jardine (2020) argues that time-dependent behaviour, as identified in Fig. 12, plays a role in post-driving set-up processes, which are remarkably pronounced in chalk.

The next stage in the experiments was to reduce the cell pressure slowly to near zero, while maintaining fixed sample height and undrained conditions. The effective stress path response was to initially increase q before migrating leftwards and following a downward $q/p' \approx 1.5$ path, reaching $p' \approx 20$ kPa after full unloading. Miniature penetrometer tests made after dismantling the specimens indicated average $S_u \approx 170$ kPa and ≈ 260 kPa in the shear zone and chalk wedge (see middle panel of Fig. 7) sections respectively: the chalk lost 90 % of its peak resistance and almost all of its mean effective stress without any drainage taking place. Fall-cone tests conducted around the tops of fully coring ALPACA piles showed putty S_u values < 20 kPa (Jardine et al., 2022), indicating that dynamic driving and shaft shearing cycles leads to still higher degrees of de-structuration in the pile shaft annuli than applied in the triaxial tests.

6. Yielding and stiffness behaviour

6.1. Large scale yielding

Figs. 3, 5, 13 and Table 4 identify the points at which the chalk underwent Y_3 yielding. A smooth elliptical Y_3 yield locus is fitted through the scattered triaxial yield points in q-p' space in Fig. 13, which also shows the oedometer yield point range and the Vinck et al.'s (2022) average tensile strength ($\sigma_t \approx 360$ kPa, equivalent to (p', q) = (-240, 360) (kPa)) from Brazilian disk tests. The Y_3 yield locus is approximately symmetrical about $p' = 2.2$ MPa, with a short-to-long radius ratio ≈ 0.55. It has a similar shape to loci identified for bonded soft rocks and residual soils

Table 4
Summary of axial strain levels (ε_a) and stress conditions (q, p') identified at intact specimens' sub-yield (Y_1) and primary yield (Y_3) states.

Test	Stage[†]	ε_{a_Y1} (%)	q_{Y1} (kPa)	p'_{Y1} (kPa)	ε_{a_Y3} (%)	q_{Y3} (kPa)	p'_{Y3} (kPa)
IC-D-63	AL	0.011	576	255	0.057	2276	821
IC-D-363	AL	0.006	407	499	0.095	4034	1707
IC-D-650	AL	0.005	360	770	0.15	3265	1738
IC-D-1000	AL	0.023	794	1265	0.16	4239	2413
IC-D-1400	AL	0.022	902	1701	0.15	3650	2617
IC-D-2000	AL	0.020	806	2269	0.088	2430	2810
IC-D-2600	AL	0.025	1017	2939	0.078	1656	3152
IC-D-3200*	IL	0.098	0	3000		NY[‡]	
	AL	0.020	798	3466	0.067	1274	3624
IC-D-7200*	IL	0.130	0	2800	0.262	0	3515
	AL	0.029	1332	7644	0.088	2703	8101
IC-D-12800*	IL	0.132	0	3000	0.238	0	4000
	AL	0.030	1825	13,408	0.095	4178	14,192

Notes:
[†] AL – Axial loading (constant σ'_h); IL – Isotropic loading (constant $q = 0$ kPa);
[‡] NY – not yield;
[*] Local strain instruments not available; axial strain based on compliance corrected external axial strains for AL stage and external volumetric strains for IL stage, assuming $\varepsilon_a = \varepsilon_{vol}/3$.

Table 5
Ratios of plastic axial and volumetric strains against total strains at Y_3 yield states.

Test	ε_{a_Y3} (%)	q_{Y3} (kPa)	$\varepsilon_a^p/\varepsilon_a^t$ (%)	$\varepsilon_{vol}^p/\varepsilon_{vol}^t$ (%)
IC-D-63	0.057	2276	21.5	−156.9
IC-D-363	0.095	4034	37.2	59.4
IC-D-650	0.15	3265	71.4	80.6
IC-D-1000	0.16	4239	37.5	72.7
IC-D-1400	0.15	3650	37.6	79.4
IC-D-2000	0.088	2430	30.6	92.5
IC-D-2600	0.078	1656	47.3	92.5
IC-D-3200	0.067	1274	52.7	82.8
IC-D-7200	0.088	2703	33.2	80.4
IC-D-12800	0.095	4178	28.6	71.5
Average (excluding IC-D-63)			41.8	79.1

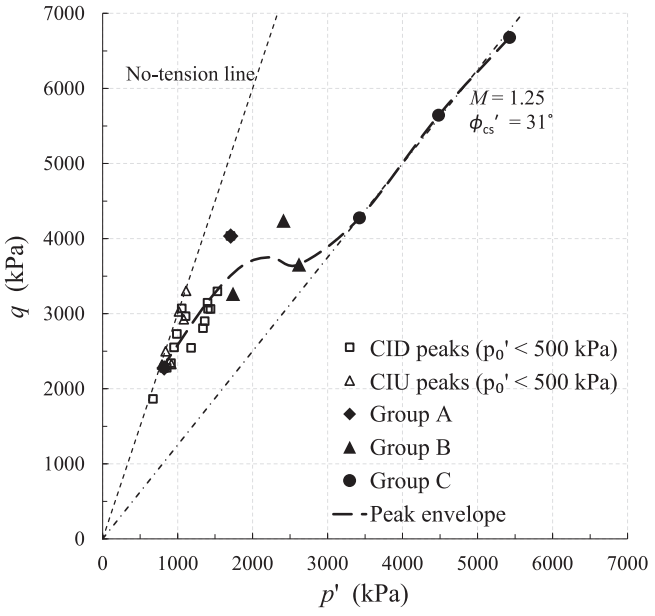

Fig. 10. Peak and ultimate shear strength envelope for intact chalk (CIU and CID peaks from Vinck (2021)).

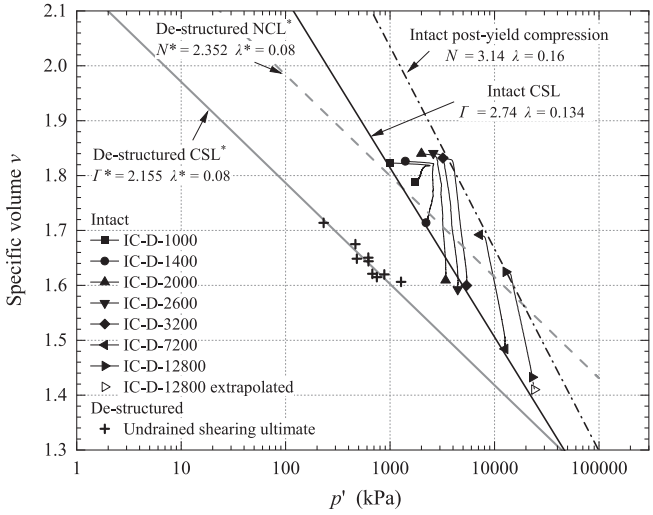

Fig. 11. Critical state relationships for intact and de-structured (Liu et al., 2022) chalk.

by Leroueil & Vaughan (1990), who argued that loci shapes and sizes depend most critically on the relative strengths of the soil grains and their inter-particle bonds.

6.2. Stiffness prior to Y_3 yielding

All shearing tests presented linear initial q-ε_a sections up to the Y_1 yield points plotted in Fig. 13 and detailed in Table 4. Y_1 yielding was located where the stress–strain (q-ε_a) response deviated from the initial linear elastic trend. A near elliptical initial Y_1 surface locating further inside the large-scale Y_3 locus is depicted for the isotropically consolidated specimens, as shown in Fig. 13. Linear regression of the pre-Y_1 trends led to the initial plateau in the equivalent secant E'_v-ε_a curves in Fig. 14. The linear-elastic plateaux span much large strain ranges than com-

monly observed for sands and clays. Group A specimens exhibited mild stiffness non-linearity with their E_v' remaining largely > 4 GPa at Y_3 yielding. Group B specimens degraded towards close Y_3 stiffnesses at similar strain levels. The degree of non-linearity increases markedly with p_0'. Smooth and continuous stiffness degradation trends were observed for the Group C specimens as they developed ductile response towards large strains.

Kuwano & Jardine (2007), Liu (2018) and Ushev & Jardine (2020) show that unbonded sands, clays and silt-dominated tills generally display small Y_1 kinematic yield loci, which often extend for just a few kPa in q-p' space and are dragged by even small movements of the current effective stress point. Their Y_1 yield surfaces tend to expand or shrink in proportion to their current p_0'; stiffness generally increases in proportion to p_0' raised to a fractional power between 0.5 and unity. In contrast, the chalk displays linear behaviour over a remarkably large region of q-p' space. Furthermore, as shown in Fig. 15, the $E_{v,max}'$ maxima show only modest (< 50 %) gains after a ten fold increase in p_0' from in-situ levels to 650 kPa. However, $E_{v,max}'$ reduces as pressures increase further and $E_{v,max}'$ remains ≈ 4 GPa over the Group C. Vinck (2021) shows that the Y_1 surface can be relocated and potentially modified by imposing sufficinetly large (drained or undrained) changes in q, followed by pause periods in which creep straining is allowed to reduce to slow rates.

Overall, the chalk's small strain stiffness behaviour appears to be controlled by both its initially cemented particulate structure and the closure of its systems of micro-to-macro fissures under elevated stresses. The cemented contacts appear to be damaged by high pressure anisotropic loading as shearing progresses between the Y_1 and Y_3 yield points identified Fig. 13 and undergo still greater damage after isotropic loading to higher p'. The destructured

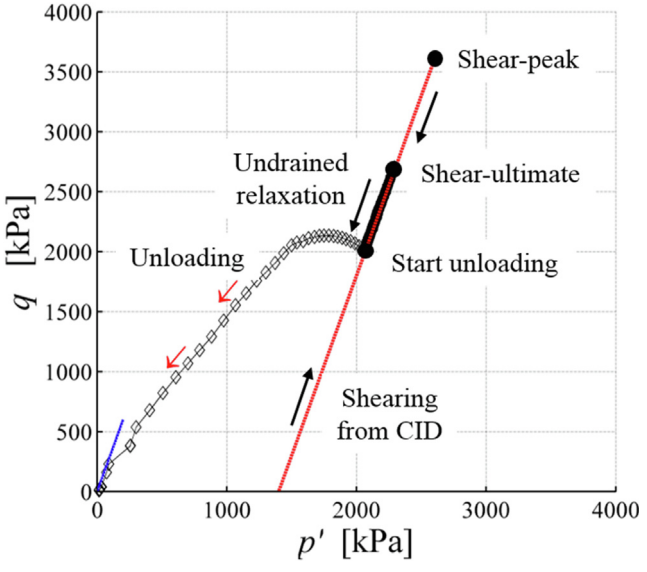

Fig. 12. Stress paths in undrained stress relaxation and unloading stages of test IC-D-1400.

chalk's stiffness gradually tends towards that expected for a unbonded silt or fine sand at similar states, as noted for calcarenite, sandstone and other cemented soils tested at high confining pressures (Cuccovillo & Coop, 1997a). For example, the $E_{v,max}' \propto f(e, \sigma_{v0}')$ trends established by Liu (2018) from high resolution tests on fine-grained Dunkirk sand predict $E_{v,max}' \approx 4.5$ GPa for the void ratio and effective stresses applied in the highest pressure chalk test (IC-D-12800), while the experiment itself indicated $E_{v,max}'$ = 6.1 GPa.

7. Establishing the Chalk's outer state boundary surface

Chalk's sedimentary conditions, its cementation in place and its long post-depositional history all contribute to its natural structure. Previous geomaterial studies have explored the impact of their genesis and subsequent history by referring behaviour under triaxial compression test conditions to that shown by soils having the same composition but tested in normally consolidated states after preparation from slurry; see for example Smith et al. (1992). The intact chalk's state paths are examined below in the same manner.

The state paths found from the drained CID tests are plotted in Fig. 16 after normalisation by M (= 1.25) and equivalent pressures (p_{cs}') defined on the critical state line of intact chalk (shown on Fig. 11) as:

$$p_{cs}' = \exp\frac{\Gamma - v}{\lambda} \quad (1)$$

with $\Gamma = 2.74$ and $\lambda = 0.134$. The void ratio changes were updated continuously along each stress path. A natural state boundary surface (SBS) is interpreted that defines the states the intact chalk can sustain before undergoing structural collapse. The final $q/(p_{cs}' \times M)$ - p/p_{cs}' paths trace towards the normalised critical state point at (1, 1).

It is also possible to normalise the test paths in terms of Hvorslev equivalent pressure $p_e'^*$ defined on the isotropic NCL* of fully de-structured chalk:

$$p_e'^* = \exp\frac{N^* - v}{\lambda^*} \quad (2)$$

with $N^* = 2.352$, $\lambda^* = 0.08$, as illustrated in Fig. 17. The normalised stress paths followed by all tests involve consolidation to p_0' levels below the isotropic (≈ 4 MPa) Y_3 value and show maximum vertical and horizontal $q/(p_e'^* \times M)$ - $p/p_e'^*$ values of ≈ 4.7 and ≈ 5.6, respectively. The paths extend out to reach far beyond local boundary surfaces (LBS*) commonly observed for reconstituted clays and silts, whose $q/(p_e'^* \times M)$ - $p/p_e'^*$ maxima usually fall ≤ 1.0, see Jardine *et al.* (2004) or Hyde et al. (2006).

As shown in Fig. 17, after achieving their maxima, which coincide with each test's Y_3 yield point, the paths rotate anticlockwise sharply and collapse inwards towards the far smaller LBS* applying to the fully de-structured chalk. The natural chalk's Local Boundary Surface (LBS) shows a normalised pattern comparable to that established, for example, by Coop (2005) for natural sands. The shear-

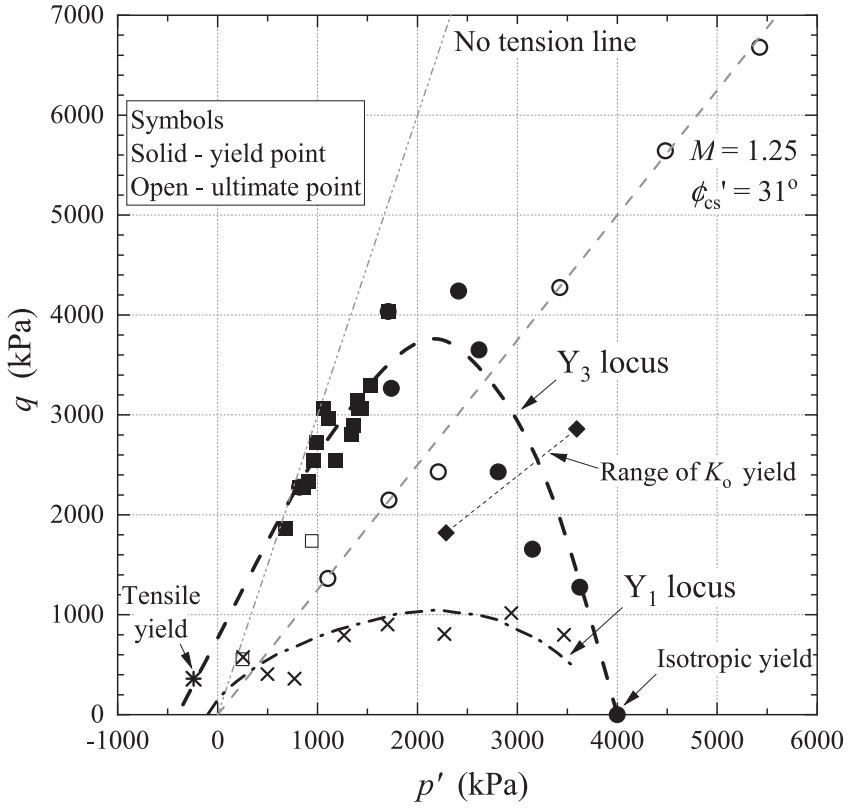

Fig. 13. Intact chalk yield stresses and interpreted pre-failure Y_1 and large-scale Y_3 loci.

ing state paths of the IC-D-12800 specimen that had been compressed far beyond its identified Y_3 yielding prior to shearing, falls well inside the natural chalk's LBS: its vertical and horizontal $q/(p'_e{}^* \times M)$ - $p/p'_e{}^*$ maxima ≈ 0.5 and ≈ 1.5 respectively.

8. Summary and conclusions

Ten main conclusions regarding the mechanical behaviour of low- to medium-density intact chalk flow from the triaxial experiments conducted under consolidation to pressures ranging from 63 kPa to 12.8 MPa.

1. The chalk's behaviour is markedly pressure dependent. When loaded from in-situ p'_0 and in-situ + 300 kPa conditions, it manifests remarkably brittle, bonded, behaviour with apparent cohesion components that contribute a large proportion of their 2.2 to 4 MPa peak deviator stresses.
2. Raising the initial isotropic p'_0 levels into the MPa range changes the chalk's shearing behaviour to being ductile and manifesting compressive volumetric straining. All experiments conducted with $p'_0 \geq 650$ kPa tended towards final critical states with $M = 1.25$, equivalent to $\phi' \approx 31°$. Bonding appears to offer only a small contribution towards the q_{ult} failure values once $p'_0 > 1.4$ MPa.
3. Specimen failure patterns also evolve from showing discontinuous bifurcation after very small axial strains ($\approx$ 0.1 %) towards bulging patterns that require axial strains up to $\approx$ 40 % to develop peak resistance.
4. Drained isotropic loading invokes tangent bulk moduli K' that initially increase until micro-fissures close fully, after which K' remains high and practically constant until large strain yielding commences and sharp K' reductions occur.
5. The intact chalk's shearing stage q-ε_a curves all manifest clear large-scale, or Y_3, yield points. An elliptical Y_3 yield locus can be established in q-p' stress space and ultimate critical state conditions identified towards which all higher-pressure tests converge.
6. The chalk's Y_3 surface has comparable characteristics to those identified for other soft rocks and bonded soils.
7. The chalk also shows very stiff initial, principally elastic, shearing behaviour. Local instrumentation allows precise measurements of vertical Young's moduli E_v', which increase modestly with pressure until they manifest their maximum (7.7 GPa) at moderate pressures (with $p'_0 = 650$ kPa) before falling to a 4 MPa plateau that extends up to the chalk's isotropic Y_1 yield point. These features differ strikingly from those shown by unbonded geomaterials.

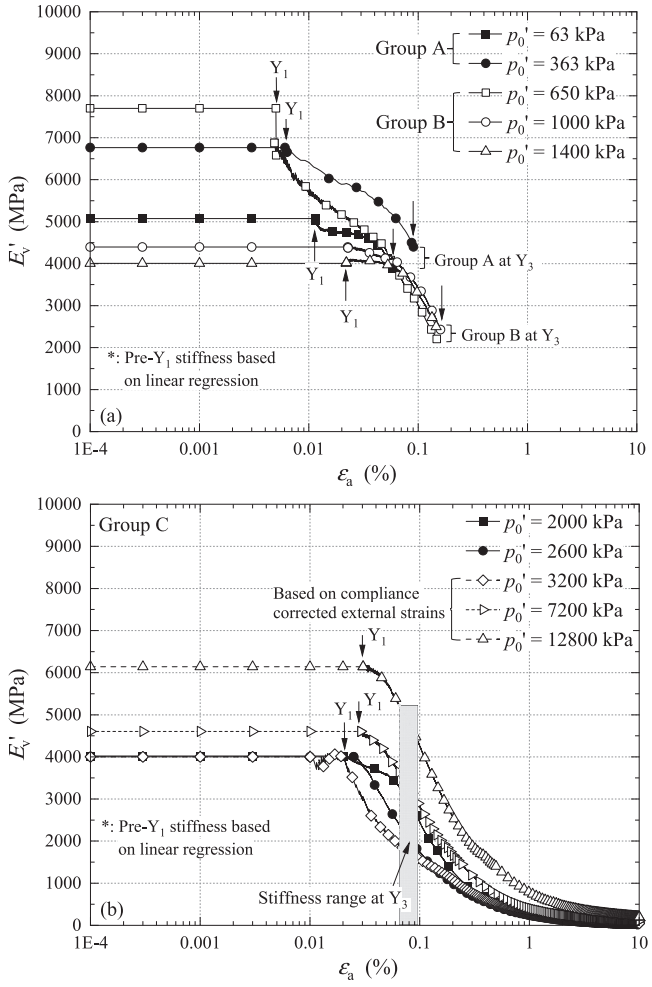

Fig. 14. Degradation trends of vertical drained secant Young's modulus: (a) Groups A and B; (b) Group C.

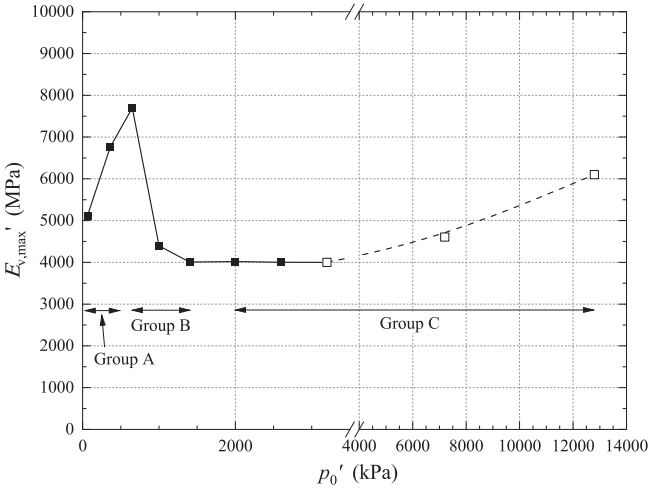

Fig. 15. Variations of maximum vertical drained Young's moduli ($E'_{v,max}$) against p'_0.

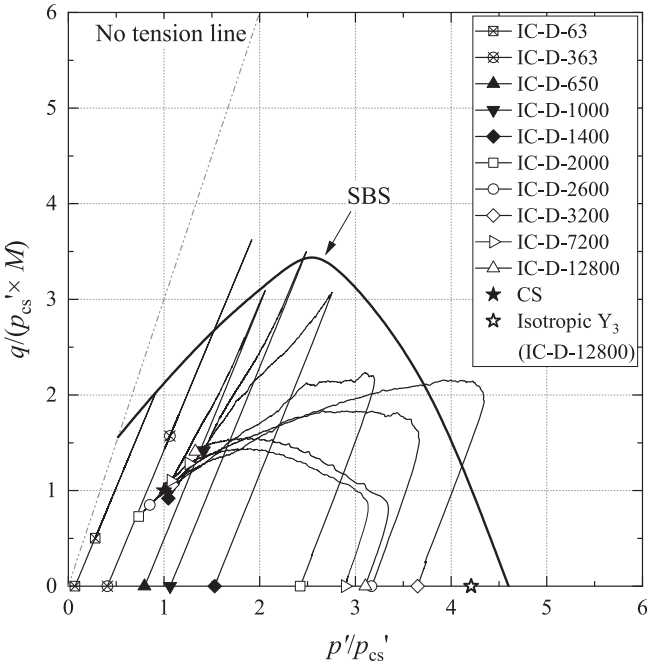

Fig. 16. Effective stress paths of intact chalk normalised by equivalent stress (p'_{cs}) defined on the critical state line of intact chalk.

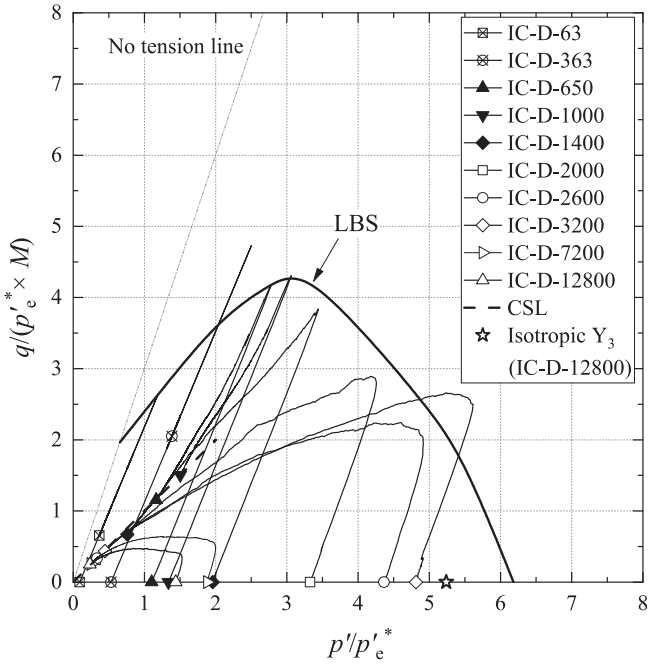

Fig. 17. Effective stress paths of intact chalk normalised by equivalent pressures (p'_e*) defined on the normal compression line of reconstituted chalk.

8. The Y_1 yield points can be combined to define a near elliptical initial Y_1 surface positioned well within the outer Y_3 locus. The Y_1 surface is kinematic, although behaviour at $p' < 300$ kPa is at least partially hysteretic and in-elastic due to the presence of micro-fissures. Stress paths that engage the Y_1 yield surface and progress outwards to the Y_3 surface showed non-linear, elastic–plastic and time-dependent behaviour.

9. The impact of the low- to medium-density chalk's bonded, yet initially high porosity, structure can be explored by normalising the shearing state paths with reference to both the chalks' critical state and intrinsic compression v-p' curves. Such normalisation reveals chalk's progressive loss of initial structure through applying shearing and isotropic compression and progressing towards a de-structured ultimate state.
10. The intact chalk's transition from remarkably brittle low-pressure behaviour to a ductile response under elevated confining pressures is broadly compatible with earlier critical state frameworks and constitutive models developed for calcarenites.

The investigation into chalk's mechanical behaviour under high pressure conditions results obtained have many pratical implications and applications. Pedone et al (2020) describe how the experiments provided crucial input into numerical analysis of the recent ALPACA and ALPACA Plus lateral axial loading tests on piles driven into the same low-to-medium density chalk.

Declaration of Competing Interest

The authors declare that they have no known competing financial interests or personal relationships that could have appeared to influence the work reported in this paper.

Acknowledgements

The joint study between Imperial College and University College London was supported by the ALPACA and APLACA Plus projects funded by the Engineering and Physical Science Research Council grant EP/P033091/1 held by Imperial College and University of Oxford (led by Professor Byron Byrne), with additional support from Atkins, Cathie Associates, Equinor, Fugro, Geotechnical Consulting Group (GCG), Iberdrola, Innogy, LEMS, Ørsted, Parkwind, Siemens and Vattenfall. Imperial College's EPSRC Centre for Doctoral Training (CDT) in Sustainable Civil Engineering (EPSRC EP/L016826/1) and the DEME Group (Belgium) supported Ken Vinck's doctoral study. Field sampling was conducted by Fugro and Socotec UK Ltd and invaluable technical support provided by Ben Boorman and Matt Wilkinson at University College London and Steve Ackerley, Graham Keefe, Prash Hirani, Stef Karapanagiotidis, Graham Nash, Gary Jones at Imperial College London.

References

Ackerley, S.K., Standing, J.R., Hosseini Kamal, R., 2016. A system for measuring local radial strains in triaxial apparatus. Géotechnique 66 (6), 515–522.

Aghakouchak, A., Sim, W.W., Jardine, R.J., 2015. Stress-path laboratory tests to characterise the cyclic behaviour of piles driven in sands. Soils Found. 55 (5), 917–928.

Altuhafi, F.N., Coop, M.R., 2011. Changes to particle characteristics associated with the compression of sands. Géotechnique 61 (6), 459–471.

Altuhafi, F.N., Jardine, R.J., Georgiannou, V.N., Moinet, W.W., 2017. Effects of particle breakage and stress reversal on the behaviour of sand around displacement piles. Géotechnique 68 (6), 546–555.

Alvarez-Borges, F., Madhusudhan, B.N., Richards, D., 2020. Mechanical behaviour of low-medium density destructured White Chalk. Géotech. Lett. 10 (2), 1–29.

D4543-19: Standard Practices for Preparing Rock Core as Cylindrical Test Specimens and Verifying Conformance to Dimensional and Shape Tolerances, 2019. ASTM International, West Conshohocken, PA. https://doi.org/10.1520/D4543-19.

Barbosa, P. M., Geduhn, M., Jardine, R. J. & Schroeder, F. C. (2017). Large scale offshore static pile tests-practicality and benefits. Society for Underwater Technology: 8th International Conference on Offshore Site Investigation and Geotechnics, Smarter Solutions for Offshore Developments, London, UK, vol. 1, pp, 644-651. https://www.ingentaconnect.com/content/sut/1hzvzd/2017/00000001/00000001/art00057;jsessionid=1ry2is2wunp8j.x-ic-live-02

Bishop, A.W., Wesley, L.D., 1975. A hydraulic triaxial apparatus for controlled stress path testing. Géotechnique 25 (4), 657–670.

Buckley, R. M., Kontoe, S., Jardine, R. J., Barbosa, P. & Schroeder, F. C. (2020b) Pile driveability in low-to-medium density chalk. Canadian Geotechnical Journal, 58 (5), 650-665. https://cdnsciencepub.com/doi/10.1139/cgj-2019-0703.

Buckley, R.M., Jardine, R.J., Kontoe, S., Barbosa, P., Schroeder, F.C., 2020a. Full-scale observations of dynamic and static axial responses of offshore piles driven in chalk and tills. Géotechnique 70 (8), 657–681.

Burland, J.B., 1990. The 30th Rankine Lecture: On the compressibility and shear strength of natural clays. Géotechnique 40 (3), 329–378.

Cerfontaine, B., Collin, F., 2018. Cyclic and fatigue behaviour of rock materials: review, interpretation and research perspectives. Rock Mech. Rock Eng. 51 (2), 391–414.

Ciantia, M.O., Arroyo, M., Sullivan, C.O., Gens, A., Liu, T., 2019. Grading evolution and critical state in a discrete numerical model of Fontainebleau sand. Géotechnique 69 (1), 1–15.

Clayton, C.R.I., 1983. The influence of diagenesis on some index properties of chalk in England. Géotechnique 33 (3), 225–241.

Coop, M. R. (2005) On the mechanics of reconstituted and natural sands. Proc., 3rd Int. Symp. on Deformation Characteristics (Di Benedetto et al. Eds), Taylor & Francis Group, London. Vol.2, 29-58. https://www.taylorfrancis.com/chapters/edit/10.1201/9780203970812-5/mechanics-reconstituted-natural-sands-coop.

Coop, M.R., 1990. The mechanics of uncemented carbonate sands. Géotechnique 40 (4), 607–626.

Cuccovillo, T., Coop, M.R., 1997a. Yielding and pre-failure deformation of structured sands. Géotechnique 47 (3), 491–508.

Cuccovillo, T., Coop, M.R., 1997b. The measurement of local axial strains in triaxial tests using LVDTs. Géotechnique 47 (1), 167–171.

Doughty, L. J., Buckley, R. M. & Jardine, R. J. (2018). Investigating the effect of ageing on the behaviour of chalk putty. Engineering in Chalk: Proceedings of the Chalk 2018 Conference (Lawrence J. A, Preene M, Lawrence U. L. and Buckley R. M. (Eds)). ICE Publishing, London, UK, pp. 695-701. https://www.icevirtuallibrary.com/doi/full/10.1680/jgeot.21.00199.

Cuccovillo, T., Coop, M.R., 1999. On the mechanics of structured sands. Géotechnique 49 (6), 741–760.

Ferreira, P.M.V., Bica, A.V.D., 2006. Problems in identifying the effects of structure and critical state in a soil with a transitional behaviour. Géotechnique 56 (7), 445–454.

Gasparre, A., Nishimura, S., Anh-Minh, N., Coop, M.R., Jardine, R.J., 2007. The stiffness of natural London clay. Géotechnique 57 (1), 33–48.

GDS (2012). GDS Introduction to soil & rock testing – Part 5: Prıncıples of testıng machıne control feedback. www.gdsinstruments.com, accessed on 10/05/2020

Hickman, R.J., Gutierrez, M.S., 2006. Formulation of a three-dimensional rate-dependent constitutive model for chalk and porous rocks. Int. J. Numer. Anal. Meth. Geomech. 31, 583–605.
Homand, S., Shao, J.F., 2000. Mechanical behaviour of a porous chalk and effect of saturating fluid. Mech Cohes. Frict. Mater. 5 (7), 583–606.
Hyde, A.F.L., Higuchi, T., Yasuhara, K., 2006. Liquefaction, cyclic mobility, and failure of silt. J. Geotech. Geoenviron. Eng. 132 (6), 716–735.
Jardine, R.J., 1992. Some observations on the kinematic nature of soil stiffness. Soils Found. 32 (2), 111–124.
Jardine, R.J., 2020. The 56th Rankine Lecture: Geotechnics, energy and climate change. Géotechnique 70 (1), 3–59.
Jardine, R.J., Symes, M.J., Burland, J.B., 1984. The measurement of soil stiffness in the triaxial apparatus. Géotechnique 34 (3), 323–340.
Jardine, R.J., Buckley, R.M., Byrne, B.W., Kontoe, S., McAdam, R.A., Andolfsson, T., Liu, T.F., Schranz, F., Vinck, K., Berthelot, P., Puech, A., Ropers, F., 2019. Improving the design of piles driven in chalk through the ALPACA research project. Rev. Fr. Geotech (158), 2.
Jardine, R. J., Buckley, R. M., Liu, T., Andolfsson, T., Byrne, B. W., Kontoe, S., McAdam, R. A., Schranz, F. & Vinck, K. (2022). The axial behaviour of piles driven in chalk, Accepted for publishing by Géotechnique.
Kohata, Y., Tatsuoka, F., Wang, L., Jiang, G.J., Hoque, E., Kodaka, T., 1997. Modelling the non-linear deformation properties of stiff geomaterials. Géotechnique 47 (3), 563–580.
Kuwano, R., Jardine, R., 2007. A triaxial investigation of kinematic yielding in sand. Géotechnique 57 (7), 563–579.
Lagioia, R. & Potts, D. M. (2011). Ground conditions due to tunnelling in hard soils. In Proceedings of 15th European Conference on Soil Mechanics and Geotechnical Engineering (Anagnostopoulos, A., Pachakis, M. & Tsatsanifos, C. (Eds)). IOS Press, pp. 1665-1670.
Lagioia, R., Nova, R., 1995. An experimental and theoretical study of the behaviour of a calcarenite in triaxial compression. Géotechnique 45 (4), 633–648.
Lagioia, R., Potts, D.M., 1999. The behaviour of shallow foundations on structured soils. Rivista Italiana di Geotecnica 4, 52–64.
Lagioia, R., Puzrin, A.M., Potts, D.M., 1996. A new versatile expression for yield and plastic potential surfaces. Comput. Geotech. 19 (3), 171–191.
Leddra, M.J., 1989. Deformation of chalk through compaction and flow. University of London (University College), PhD Thesis,.
Leroueil, S., Vaughan, P.R., 1990. The general and congruent effects of structure in natural soils and weak rocks. Géotechnique 40 (3), 467–488.
Liu, T. (2018) Advanced laboratory testing for offshore pile foundations under monotonic and cyclic loading, PhD thesis, Imperial College London
Liu, T., Ahmadi-Naghadeh, R., Vinck, K., Jardine, R. J., Kontoe, S., Buckley, R. M and Byrne, B. W. (2022). An experimental investigation into the behaviour of de-structured chalk under cyclic loading. Ahead of Print in Géotechnique https://www.icevirtuallibrary.com/doi/full/10.1680/jgeot.21.00199.
Lord, J. A., Clayton, C. R. L. & Mortimore, R. N. (2002). Engineering in chalk, CIRIA, C574.
Mortimore, R.N., 2012. The 11th Glossop Lecture: making sense of chalk: a total-rock approach to its engineering geology. Q. J. Engng Geol. Hydrogeol. 45 (3), 252–334.
Pedone, G., Kontoe, S., Zdravkovic, L., Jardine, R.J., 2020. Supergen ORE Flexible Funding Research Project ALPHA: Numerical analysis of laterally loaded piles driven in chalk. Final Report, Imperial College London, September, p. 2020.
Potts, D.M., Jones, M.E., Berget, O.P., 1988. Subsidence above the Ekofisk oil reservoirs. 5th Int. Conf. On Behaviour of Offshore Structures. Tapir, Trondheim, Publisher, pp. 113–127.
Risnes, R., 2001. Deformation and yield in high porosity outcrop chalk. Phys Chem Earth Sci 26 (1-2), 53–57.
Smith, P.R., Jardine, R.J., Hight, D.W., 1992. The yielding of Bothkennar clay. Géotechnique 42 (2), 257–274.
Tatsuoka, F., Jardine, R. J., Lo Presti, D., Di Benedetto, H. & Kodaka, T. (1999) Theme lecture: Characterising the pre-failure deformation properties of geomaterials. Proceedings of the 14th International Conference on Soil Mechanics and Foundation Engineering, Hamburg. pp: 2129-2164.
Ushev, E., Jardine, R., 2020. The behaviour of Bolders Bank glacial till under undrained cyclic loading. Géotechnique 72 (1), 1–19.
Vinck, K., 2021. Advanced geotechnical characterisation to support driven pile design at chalk sites. Imperial College London, PhD thesis,.
Vinck, K., Liu, T., Jardine, R. J., Kontoe, S., Ahmadi-Naghadeh, R., Buckley, R. M., Byrne, B. W., Lawrence, J., Mcadam, R. A. & Schranz, F. (2022) Advanced in-situ and laboratory characterisation of the ALPACA chalk research site. Ahead of Print in Géotechnique. https://www.icevirtuallibrary.com/doi/epdf/10.1680/jgeot.21.00197.
Zimmerman, R.W., 1985. The effect of microcracks on the elastic moduli of brittle materials. J. Mater. Sci. Lett. 4 (12), 1457–1460.